Electronic Supplementary Material (ESI) for CrystEngComm

Hierarchical *rh*-In_2O_3 crystals derived from InOOH counterparts and their sensitivity to ammonia gas

Haihui Jiang,[a] Lichun Zhao,[a] Ligang Gai,*[a] Li Ma,[a] Yun Ma[a] and Mei Li[b]

[a]*Key Laboratory of Fine Chemicals in Universities of Shandong, School of Chemistry & Pharmaceutical Engineering, Shandong Polytechnic University, Jinan 250353, People's Republic of China*

[b]*School of Material Science & Engineering, Shandong Polytechnic University, Jinan 250353, People's Republic of China*

Supplementary Material

S1. Illustration of a gas sensor

Fig. S1 shows the schematic drawing of a gas sensor.

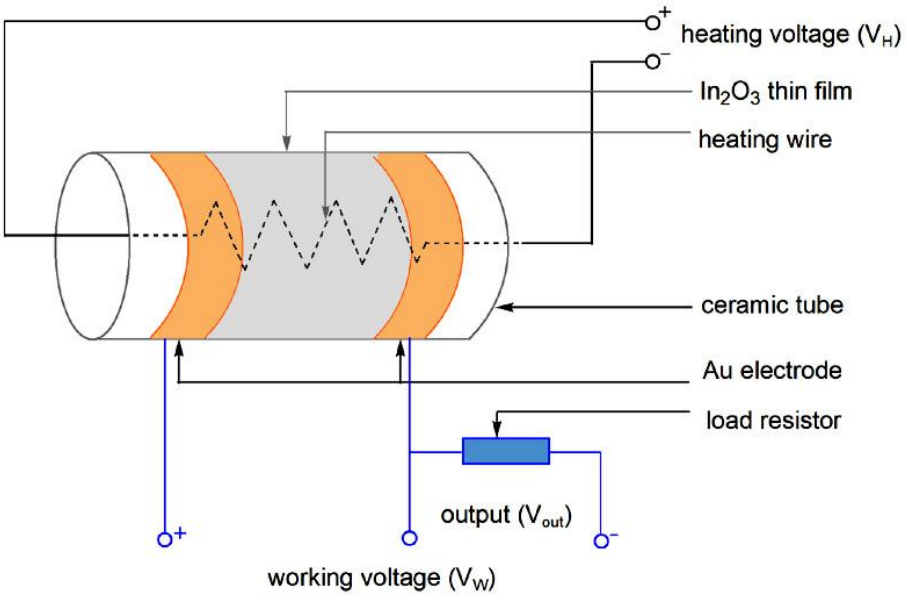

Fig. S1 Schematic drawing of a gas sensor.

S2. FTIR spectrum

Fig. S2 shows the FTIR spectrum of the *rh*-In_2O_3 sample. The peaks around 3430 and 1627 cm^{-1} are due to the surface adsorbed water. The peaks centered at 502 and 443 cm^{-1} correspond to the In–O vibrations of *rh*-In_2O_3.

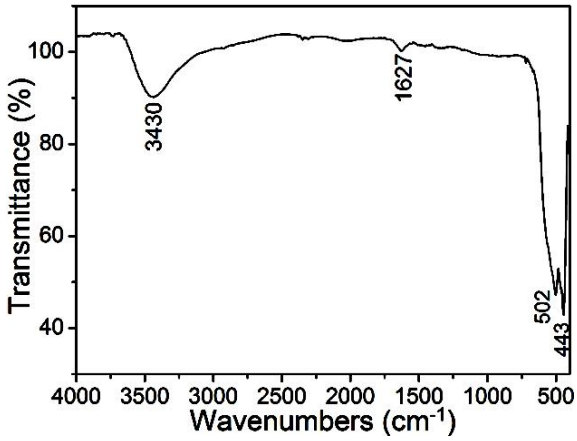

Fig. S2 FTIR spectrum of the *rh*-In_2O_3 sample.

S3. Size and morphology of InOOH counterparts

Fig. S3 shows the size and morphology of the InOOH hierarchical crystals. It is apparent that there are many nanoparticles with size smaller than 50 nm attached on the rod matrix. Lattice spacing of *ca.* 2.78 Å in Fig. S3f agrees well with the d_{101} value for orthorhombic InOOH, revealing good crystallinity of the InOOH hierarchical crystals.

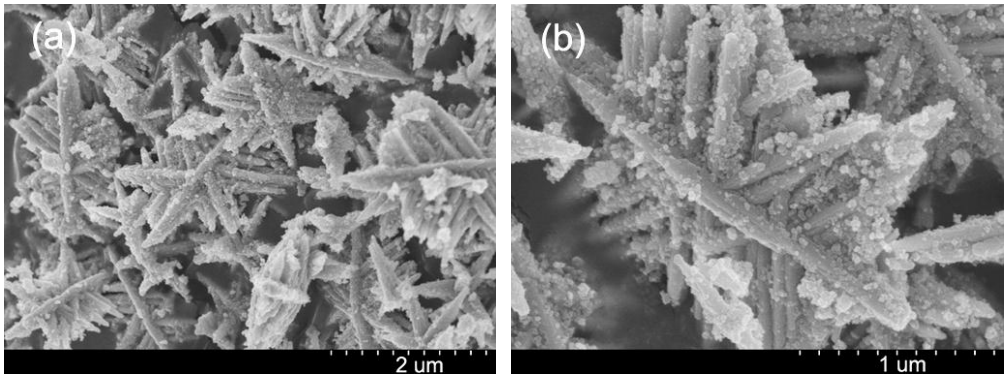

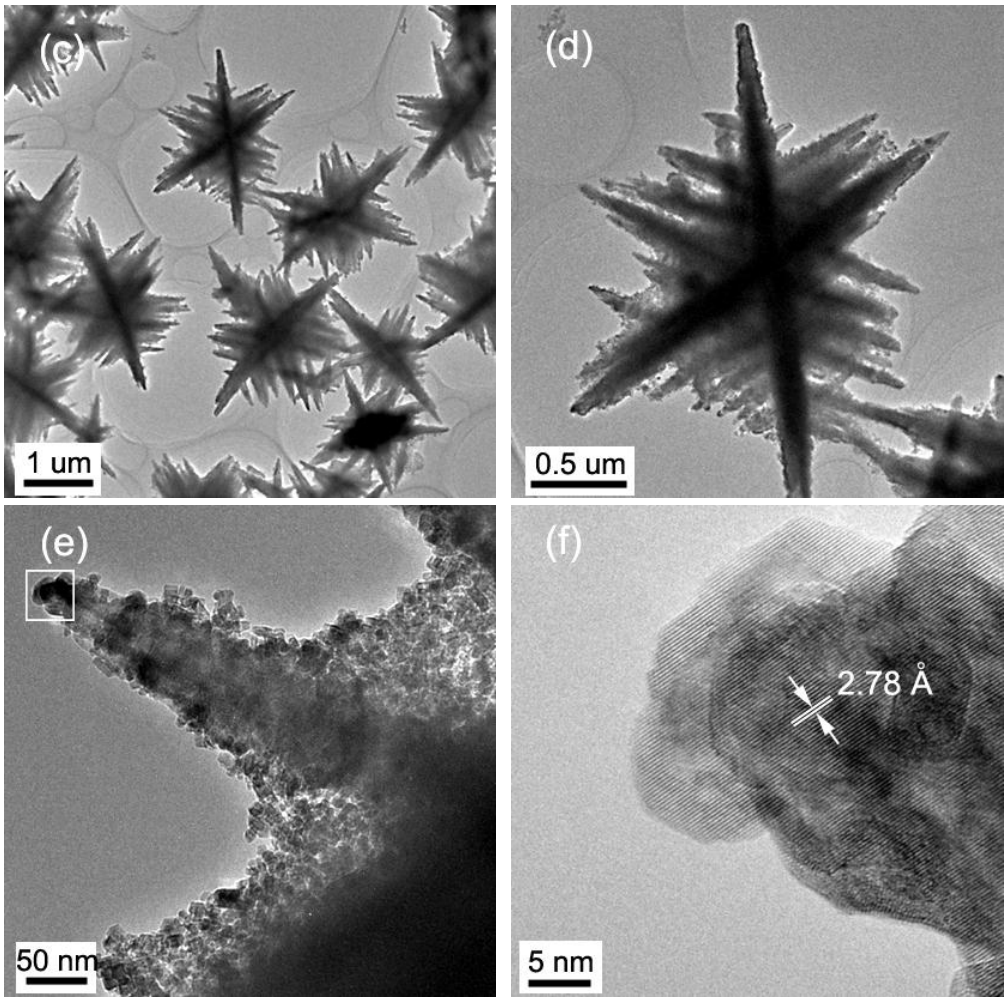

Fig. S3 SEM (a and b) and (c to f) images of InOOH hierarchical crystals: (a) Low-magnification; (b) High-magnification; (c and d) Low-magnification; (e) High-magnification; (f) High-resolution TEM image of the squared area in e.

S4. Effect of the water content on the samples prepared in EG solution

Fig. S4 shows the XRD patterns of the samples prepared in control experiments. In the EG solution with water content not more than 6.5 vol%, pure *c*-In_2O_3 nanoparticles (Fig. S4a to c) were obtained. All the diffraction peaks marked in Fig. S3c can be indexed to (211), (222), (400), (411), (332), (431), (440), (611), and (622) planes of *c*-In_2O_3 (JCPDS no. 71-2195). Also, the crystallinity of the *c*-In_2O_3 samples increases with the increase of water content in the range of 0–6.5 vol%. When the

water content lies in the range of 6.5–12.9 vol%, mixed phase appears containing *c*-In_2O_3 and orthorhombic InOOH (Fig. S4d). It is worth noting that pure InOOH crystals can only be acquired with water content ranging from 13 to 22.6 vol% (Fig. S4e). With water content in the range of 22.6–29 vol%, mixed phase appears in a InOOH/$In(OH)_3$ binary structure (Fig. S4f). When the water content is more than 30%, pure cubic $In(OH)_3$ crystals (Fig. S4g) can be obtained. All the diffraction peaks marked in Fig. S4g can be indexed to (200), (220), (013), (222), (400), (420), (422), (440), (442), (620), (622), and (046) planes of *c*-$In(OH)_3$ (JCPDS no. 76-1463).

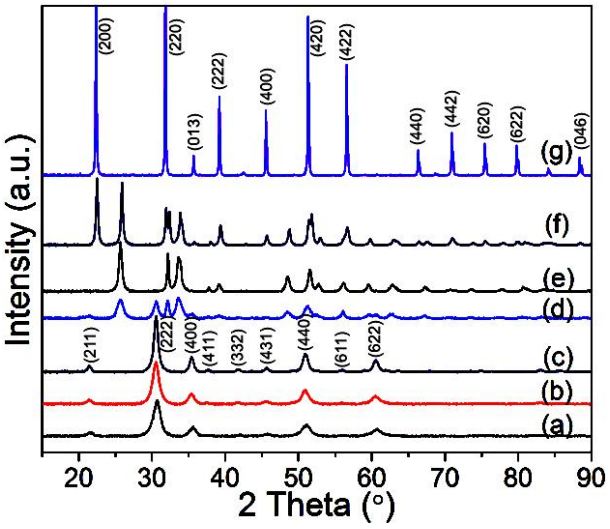

Fig. S4 XRD pattern of the samples prepared at 200 °C for 12 h in EG solution with volume percentage of water: (a) 0; (b) 3.2%; (c) 6.5%; (d) 9.7%; (e) 16%; (f) 23%; (g) 33%.

Fig. S5 shows the size and morphology of the pure *c*-In_2O_3 (Fig. 5Sa to c) and $In(OH)_3$ samples (Fig. 5Sd). The *c*-In_2O_3 nanocrystals with size less than 50 nm tend to aggregate to form hierarchical structures. No apparent difference occurs in the three *c*-In_2O_3 samples with increasing water content in EG solution. The $In(OH)_3$ sample is mainly composed of relatively large cubes with size ranging from 60 to 190 nm, and there are many relatively small nanocubes and/or nanoparticles attaching on the large

cubes. The small nanocubes and/or nanoparticles have a size range of 10–40 nm.

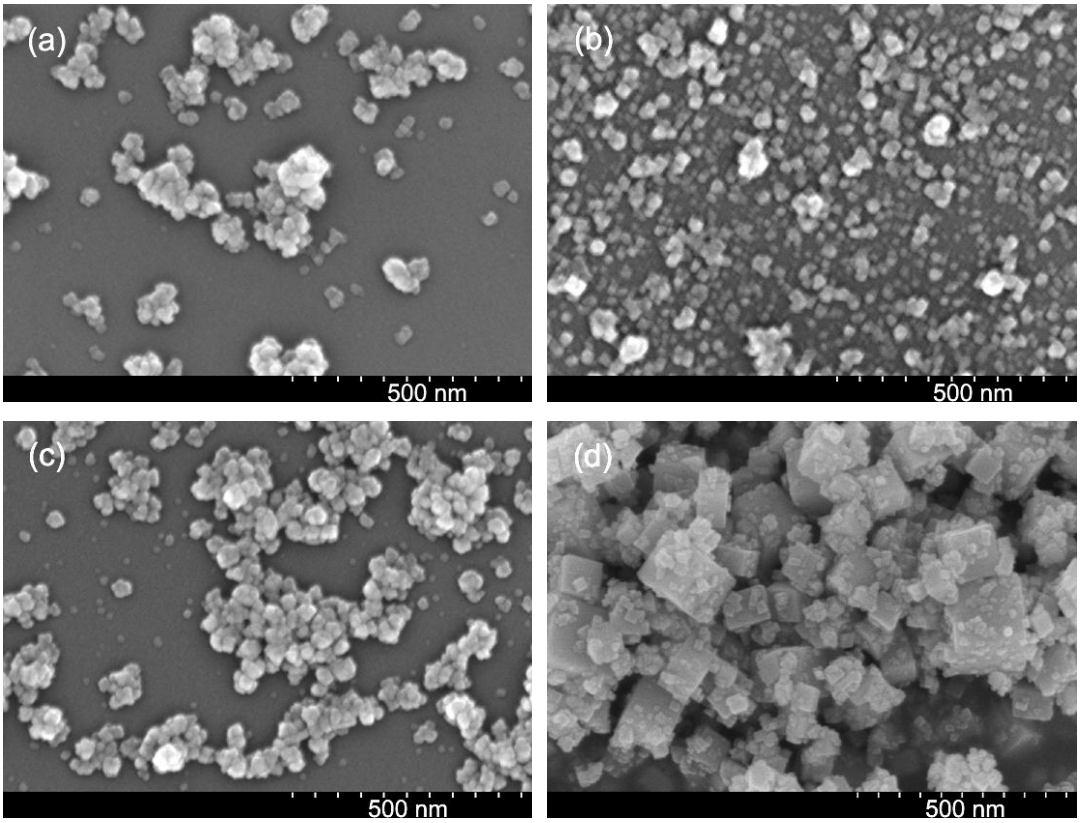

Fig. S5 SEM images of the samples prepared at 200 °C for 12 h in EG solution with volume percentage of water: (a) 0; (b) 3.2%; (c) 6.5%; (d) 33%.

S5. Effect of the solvent on the products

In an ethanol solution with water content of 3.2 vol%, a mixed phase in InOOH/*c*-In_2O_3 form occurs with InOOH crystals in majority (Fig. S6). Apart from the peaks marked with asterisks denoting the phase of *c*-In_2O_3, all the other peaks arise from InOOH (JCPDS no. 71-2284). The sample is dominated by short nanorods with an average diameter of *ca.* 20 nm. The aspect ratio of the rods is *ca.* 2–3 (Fig. S7).

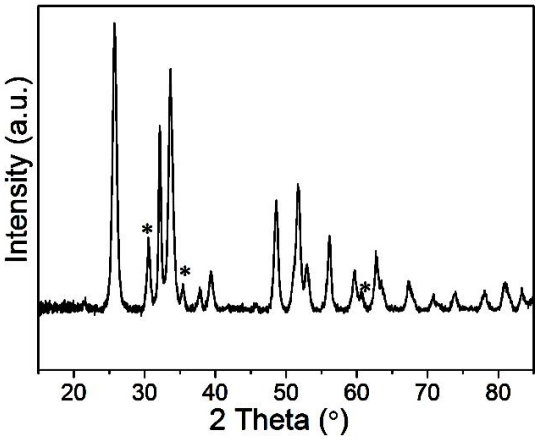

Fig. S6 XRD pattern of the sample prepared in an ethanol solution with a water content of 3.2 vol%. The peaks marked with asterisks denote *c*-In_2O_3.

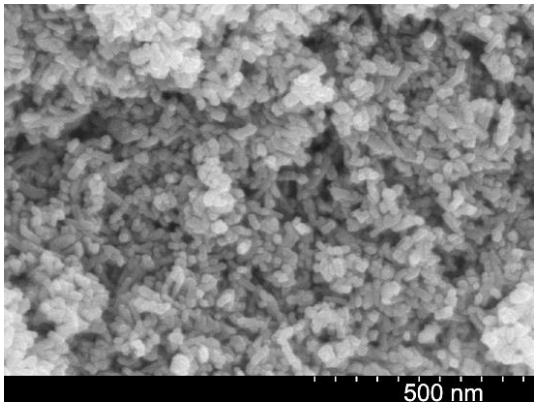

Fig. S7 SEM image of the sample prepared in an ethanol solution with a water content of 3.2 vol%.

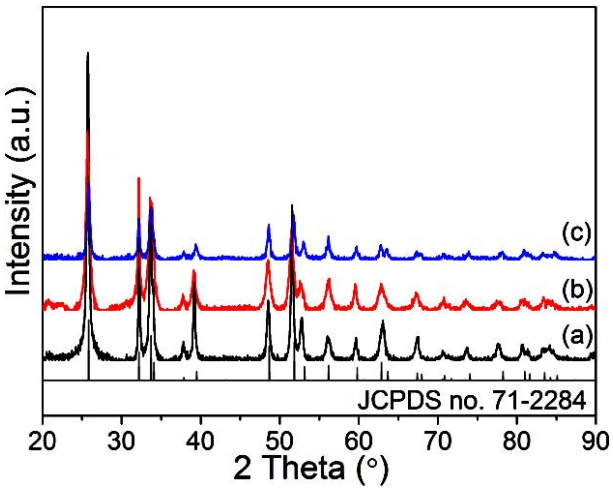

Fig. S8 XRD patterns of the samples prepared at 200 °C for 12 h in: (a) glycerol with 25.8 vol% H_2O; (b) DEG with 2.58 vol% H_2O; (c) TEG with 2.58 vol% H_2O.

Fig. S8 shows the XRD patterns of the InOOH samples separately prepared in glycerol, diethylene glycol (DEG), and triethylene glycol (TEG) solutions. In a typical synthesis with glycerol, 8 mL of distilled water was added into 23 mL of glycerol with agitation to form a clear solution. Then, 0.44 g (2 mmol) of $InCl_3$ and 1.77 g (13 mmol) of $NaAc{\cdot}3H_2O$ were added into the mixture. The mixture was vigorously stirred at room temperature for 1 h, and then transferred into a Teflon-lined autoclave (40 mL capacity). The autoclave was heated at 200 °C for 12 h, and allowed to cool to room temperature. The resulting product was collected by filtration and washed thoroughly with distilled water and anhydrous ethanol, and finally dried in a vacuum oven at 40 °C for 10 h. In the case of using DEG or TEG as the reaction medium, 0.8 mL of distilled water and 30.2 mL of DEG or TEG were used under otherwise identical conditions.

It is apparent that pure InOOH crystals can be acquired with the three kinds of polyols (Fig. S8). A noteworthy point is that, to acquire pure InOOH crystals, the volume percentage of water (21–29 vol%) in glycerol solution is much higher than that of 1.9–3.2 vol% in DEG and/or TEG solutions.

S6. Effect of the duration time on the phase of the samples

The phase and composition of the samples prepared with duration time of 1–4.5 h were determined by the XRD technique (Fig. S9). The sample obtained at the duration time of 1 h is nearly pure *c*-$In(OH)_3$ (Fig. S9a). All the diffraction peaks marked in Fig. S8a can be indexed to (200), (220), (400), (420), and (422) planes of *c*-$In(OH)_3$ (JCPDS no. 76-1463). A noteworthy point is that the diffraction peaks corresponding

to InOOH component begin to occur and to increase in intensity, whereas the peaks belonging to *c*-$In(OH)_3$ component decrease in intensity as the duration time increases from 1 to 4.5 h, (Fig. S9b and c).

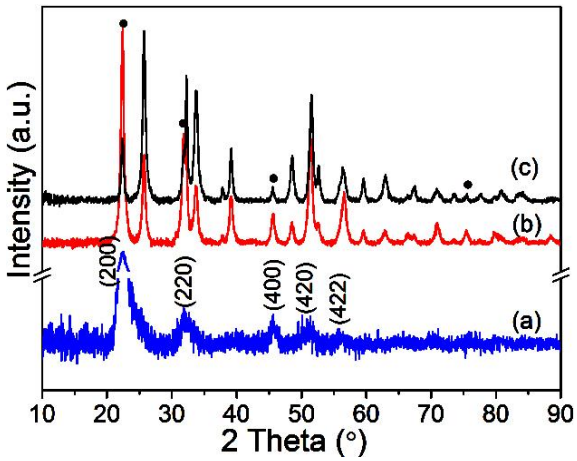

Fig. S9 XRD patterns of the samples prepared at 200 °C with duration time of: (a) 1 h; (b) 2.5 h; (c) 4.5 h. The black dots marked in spectra b and c denote *c*-$In(OH)_3$.

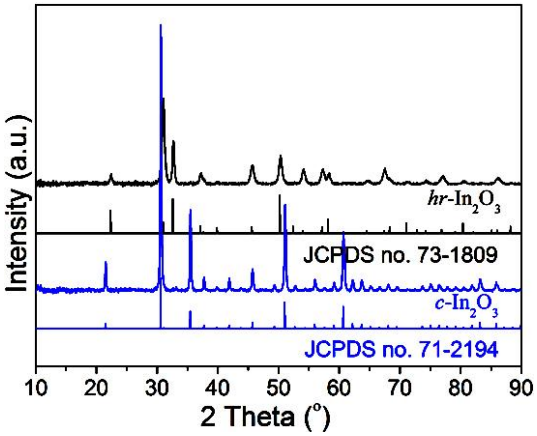

Fig. S10 XRD patterns of *hr*-In_2O_3 and *c*-In_2O_3 samples obtained by annealing InOOH counterparts at different temperatures.

S7. Structure and morphology of *c*-In_2O_3 crystals

Fig. S10 shows the structure of the *c*-In_2O_3 sample obtained by annealing the hierarchical InOOH counterparts. It is apparent that the crystallinity of the *c*-In_2O_3 sample is higher than that of the *hr*-In_2O_3 sample. This conclusion is based on the

stronger diffraction intensity of the former compared to that of the latter (Fig. S10), due to the higher anneal temperature for *c*-In_2O_3 (650 °C) compared to that for *hr*-In_2O_3 (500 °C). The diffraction data of the *c*-In_2O_3 sample agree well with those reported in literature (JCPDS no. 71-2194).

S8. Plots of $(\alpha hv)^{1/2}$ *versus hv* for the In_2O_3 samples

Fig. S11 shows the plots of $(\alpha hv)^{1/2}$ *versus hv* from the UV-Vis absorbance spectral data regarding to *rh*-In_2O_3 and *c*-In_2O_3. The intercept along the linear parts of the two plots places the indirect band transitions at the same position of 2.52 eV, indicating that the plots of $(\alpha hv)^{1/2}$ *versus hv* obscure the discrepancy in band structure of the *rh*-In_2O_3 and *c*-In_2O_3 samples.

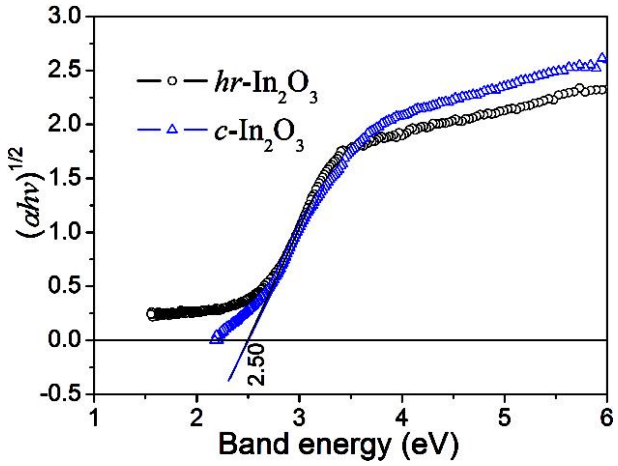

Fig. S11 Plots of $(\alpha hv)^{1/2}$ *versus hv* from the UV-Vis absorbance spectral data regarding to In_2O_3.

S9. Sensitivity of the sensors as a function of temperature

Fig. S12a shows the variation in sensitivity to 5 ppm NH_3 as a function of temperature with respect to the sensors made from *rh*-In_2O_3 and *c*-In_2O_3 samples. It is apparent that the sensitivity of the sensor constructed with *rh*-In_2O_3 hierarchical crystals is higher than that of the sensors separately made from *c*-In_2O_3 analogues and *c*-In_2O_3 nanoparticles, especially for the sensor working at the temperature of 300 °C. Also,

although the sensor made from *c*-In_2O_3 nanoparticles offers good reproducibility and small deviations for five replicates working at the temperature of 300 °C. (Fig. S12b), the response time of 25 s is much higher than that of *ca.* 3 and 19 s for the sensors based on *rh*-In_2O_3 and *c*-In_2O_3 hierarchical crystals, respectively.

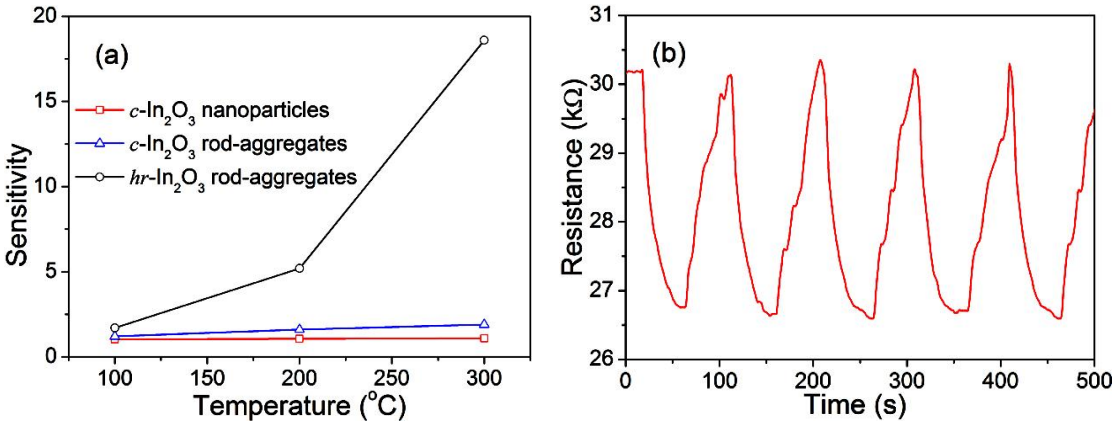

Fig. S12 (a) Variation in sensitivity to 5 ppm NH_3 of the sensors as a function of temperature; (b) Response curve to 5 ppm NH_3 of the sensor made from *c*-In_2O_3 nanoparticles working at the temperature of 300 °C.